Observational evidence for cylindrically oriented zonal flows on Jupiter

Y. Kaspi, E. Galanti, R S Park, K. Duer, N. Gavriel, D. Durante, L. Iess, M. Parisi, D. Buccino, T. Guillot, et al.

Observational evidence for cylindrically oriented zonal flows on Jupiter

Y. Kaspi, E. Galanti, R. S. Park, K. Duer, N. Gavriel, D. Durante, L. Iess, M. Parisi,
D. Buccino, T. Guillot, D. J. Stevenson and S. J. Bolton

June 20, 2023

The atmospheric dynamics of Jupiter are dominated by strong zonal winds engulfing the planet. Since the first gravity measurements of Juno at Jupiter, the low-degree gravity harmonics ($J_3 - J_{10}$) have been used to determine the depth and structure of the zonal winds observed at the cloud level, limiting the inference on the deep flows to the wide latitudinal structure of these harmonics. Here, using constraints on the dynamical contribution to gravity at high latitude, we present the gravity harmonics up to J_{40}. We find an excellent correlation between these measurements and the gravity harmonics resulting from the observed cloud-level winds extending inward cylindrically to depths of $\sim 10^5$ bar (3000 km). These measurements provide direct evidence that the flows penetrate inward along the direction of the spin axis, confirming the cylindrical nature of the flow, which has been postulated theoretically since the 1970s. Furthermore, this detailed new gravity spectrum allows to quantify the contribution of the various jets to the gravity signal, showing the dominance of the strong flows around latitude 20° in both hemispheres.

Introduction

Jupiter's atmosphere is dominated by strong east-west zonal jetstreams, which are strongly tied to the planet's iconic red and white stripes[1,2]. There are 6 pairs of east-west jets in each hemisphere with peak velocities ranging between -50 and 140 m s^{-1}, and located between latitudes 15° and 65° in both hemispheres (Fig. 1a,c). Equatorward, there is an eastward flow with velocities of ~ 100 ms^{-1}, which is super-rotating within six degrees of the equator[3]. Poleward, the jets disappear and the dynamics turn to be dominated by vortices all the way to the poles. At both poles, there are powerful cyclones with a diameter of ~ 4000 km, surrounded by similar sized circumpolar cyclones (8 in the north and 5 in the south[4,5]). This picture has become clearer since the arrival of NASA's Juno mission to Jupiter in 2016[6], and as the mission continues orbiting the planet, with the closest approach moving closer to the north pole every orbit, more information is continuously accumulated. Currently, more than seven years into the mission, the cumulative data allows revolutionizing our understanding of the atmospheric dynamics of Jupiter[7,8].

One of the first results that emerged from Juno, has been the measurement of the north-south asymmetry in Jupiter's gravitational field[9]. This has been attributed to the observed north-south asymmetry in Jupiter's cloud-level winds[10], and matched pre-Juno theoretical estimates for the gravity signature as function of flow depth[11]. The precise measurements by the Juno mission, based on tracking of the Doppler shift of a radio signal as the spacecraft is orbiting the planet, allowed determining that the observed cloud-level flows extend roughly 3000 km (10^5 bar) beneath the observed cloud-deck of Jupiter[10]. This analysis was based on analyzing the odd gravity harmonics (J_3, J_5, J_7 and J_9), and the results matched also the low-degree even harmonics J_6, J_8 and J_{10} after subtracting the contribution from the internal density structure[12,13]. These results were also found to be consistent with constraints coming from secular variations of Jupiter's magnetic field[14,15,16], and the possibility of a stable layer acting to decay the flow at this depth[17]. In this study, using constraints on the high-degree gravity harmonics at high latitudes (see below), we present the gravity harmonics up to degree 40 (ED Table 1), which we find to correlate well with the calculated wind-induced gravity harmonics. This strengthens the conclusion that indeed the measured gravity anomalies are caused by the winds observed at the cloud-level extending inward. Moreover, the analysis provides direct observational evidence that the cloud-level winds extend inward along the direction of the spin axis as has been suggested in theoretical studies[18,19].

The gravity harmonic coefficients (J_n, see Methods) are an integrated measure of the planetary density distribution projected on a Legendre polynomial basis function. These traditionally have been used to understand the planetary shape and radial density distribution of nearly spherical objects[21,22,7]. The high precision gravity measurements of the Juno mission[23,9] enabled detecting small variations in the gravity field due to the flows circulating the planet, which create a geostrophic density anomaly that imprints the gravity signal[24,10]. Thus, the density can be separated into a static component, which is to leading order north-south symmetric (as the mean radial density profile has no hemispherical asymmetries), and a dynamical component due to the flows, which is north-south asymmetric[11]. The static component of the gravity harmonics decreases rapidly with increasing degree, while the dynamical component remains roughly the same magnitude for high harmonics due to the latitudinal variability of the wind induced density variations[25]. This results in the gravity signal beyond J_{10} being fully due to the dynamics (ED Fig. 1). Until the current analysis, gravity measurements could resolve individual harmonics up to J_{10}, meaning that determination of the depth of the flow could be done either by the low degree odd harmonics (J_3, J_5, J_7 and J_9) or by subtracting the static component of the even harmonics ($J_6 - J_{10}$), based on interior structure models[12], from the measurements. Thus, by coincidence, it hap-

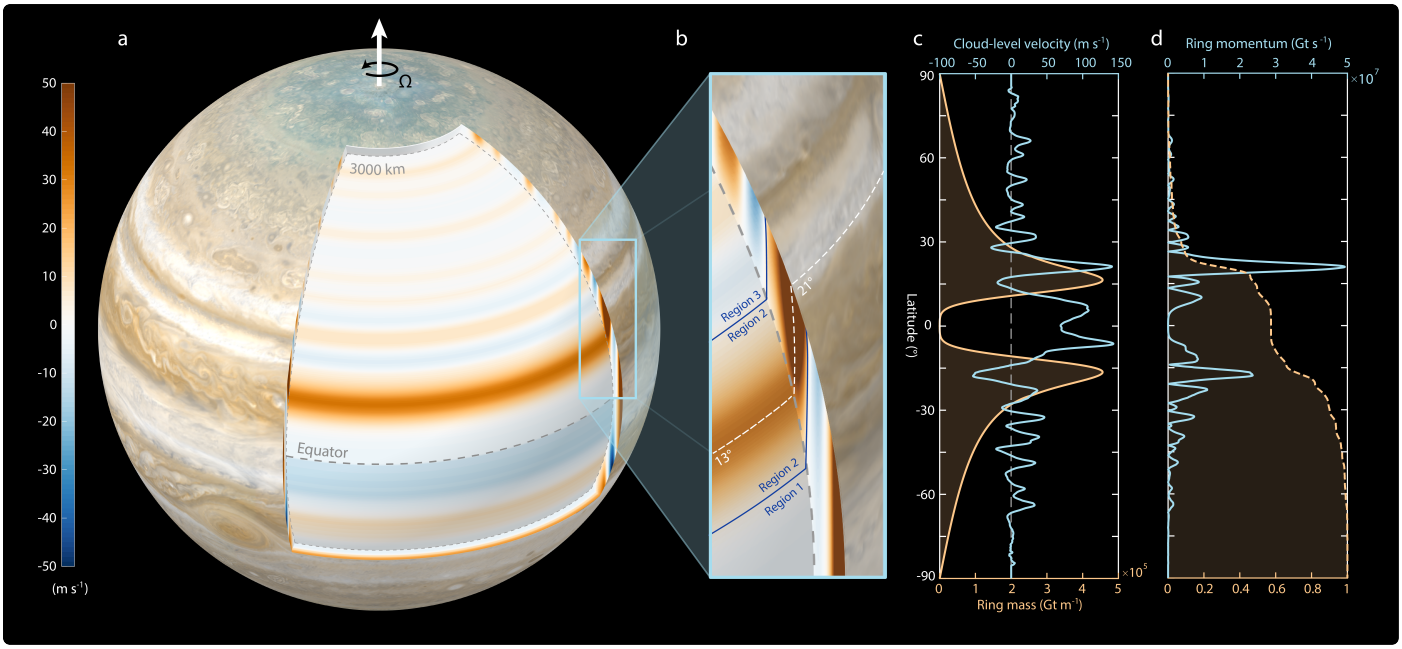

Figure 1: **Jupiter's zonal flows and their cylindrical orientation. a.** 3D illustration of Jupiter's clouds and wind field (color). The wind field is the zonally averaged zonal wind[20] ($\mathrm{m\,s^{-1}}$) projected inwards in a direction parallel to the axis of rotation and decays in the radial direction according to the best-fit solution based on the Juno gravity measurements[10]. The inner shell represents the winds at a depth of 3000 km. The clouds picture is a combination of Juno and Cassini visible light images; Credit: NASA / JPL-Caltech / SSI / SWRI / MSSS / ASI / INAF / JIRAM / Björn Jónsson. **b.** An inset of the pale blue rectangle from panel a, showing the cylindrical nature of the strong 21°N cloud-level jet that projects to latitude 13°N at a depth of 3000 km (Region 2). The white dashed line represents the location of its maximum velocity at all depths. The region equatorward (Region 1, outside the tangent cylinder) contains mostly shallow flows, and the region poleward (Region 3) has weaker jets, which become weak (< 10 m $\mathrm{s^{-1}}$) at 3000 km. **c.** The zonal mean zonal wind at the cloud level[20] (blue), and an estimation of the mass (per meter of a latitude ring) participating in the zonal flows, extending downward in the cylindrical direction (orange, Methods M5). **d.** The multiplication of the absolute value of the two curves of panel c (blue), giving an estimate of the wind induced momentum of each cylindrical ring (per meter in the meridional direction), and the cumulative integral (normalized by the total shell momentum) of the blue curve, starting from the north pole (orange).

pened that the Juno measurement sensitivity and the degree where the spectrum becomes purely dynamical (for both even and odd) were at J_{10}. Here, we expand the measured gravity spectrum to much higher degree allowing to better resolve the dynamical effects.

Results

Analysis of the high-harmonic gravity signal

The Juno spacecraft closest approaches to Jupiter are at low and midlatitudes, and thus the Juno gravity data sensitivity is saturated near the poles, limiting the number of gravity harmonics that can be resolved. To overcome this limitation, we take advantage of the fact that the zonal flows at high latitudes are weak[26], and that the background interior mass distribution is not expected to contribute to the gravity harmonics beyond J_{10}[25], and constrain the zonal harmonics beyond J_{12} to less than 1 mGal at high latitudes (Methods, M1). This allows resolving the gravity harmonics up to J_{40} under this assumption. In other words, spatial constraints were applied near the poles so that the recovered high-degree J_n represent the gravity in the latitude band between 40°S and 70°N where the Juno sensitivity to jovian gravity is highest. This constraining technique is often used when there is incomplete spatial coverage[27,28].

With this assumption, the gravity harmonics can be measured to high-degree (Fig. 2a, black), demonstrating a wavy pattern. This assumption does not affect the low degree harmonics ($J_2 - J_{10}$) measured without this assumption[29]. Equivalently, the gravity harmonics resulting from the dynamics (Fig. 2a, red), are calculated by extending the cloud-level winds inward along the direction of the spin axis, and optimizing their vertical profile, so that the wind induced gravity harmonics match the measured low-degree odd gravity harmonics (J_3, J_5, J_7 and J_9) as done in previous studies[10,13]. The optimization is done using the adjoint method[30], and the relation between the wind structure and the density anomalies used for calculating the J_n is done via thermal wind (TW) balance[31,3,24] (Methods, M2 & M3). Fig. 2a shows that the constrained measurements match remarkably well the dynamical values up to J_{40} (correlation of 0.87), indicating that, with very high likelihood, the measured gravity harmonics are due to the winds. It is also evident that this match is associated with the wavy pattern of the signal (explained below), which decreases in power for the higher degrees and has a wavelength of $5-6$ harmonic degrees. Note the gravity harmonics are pre-

sented on a linear scale, unlike the traditional presentation of the gravity harmonics on a log-scale (ED Fig. 1)[25], which further emphasizes the strong match to the measurements.

The short rotation period of the planet (9.92 hours) and the large scale of the dynamics result in geostrophic dynamics[3]. This also implies that theoretically, and if the dynamics are also barotropic, the zonal flow is expected to extend inward along the direction of the axis of rotation. This has been discussed theoretically since the early papers about Jupiter's dynamics[18,32], demonstrated in laboratory experiments[33], 3D numerical simulations[19,34,35,36], and used in numerous theoretical studies[37,38], but never confirmed observationally. The barotropic nature of the flows is known from the fact that they decay inward very gradually over several thousand kilometers[10], and thus although not purely barotropic, the decay is weak enough so that nearly barotropic dynamics apply[39,14], and thus the flow is expected to be aligned with the axis of rotation[31]. Here we take advantage of the new knowledge of the high-degree gravity harmonics to show observational evidence for the alignment of the zonal flows with the axis of rotation. Fig. 2b shows the same as in Fig. 2a, but

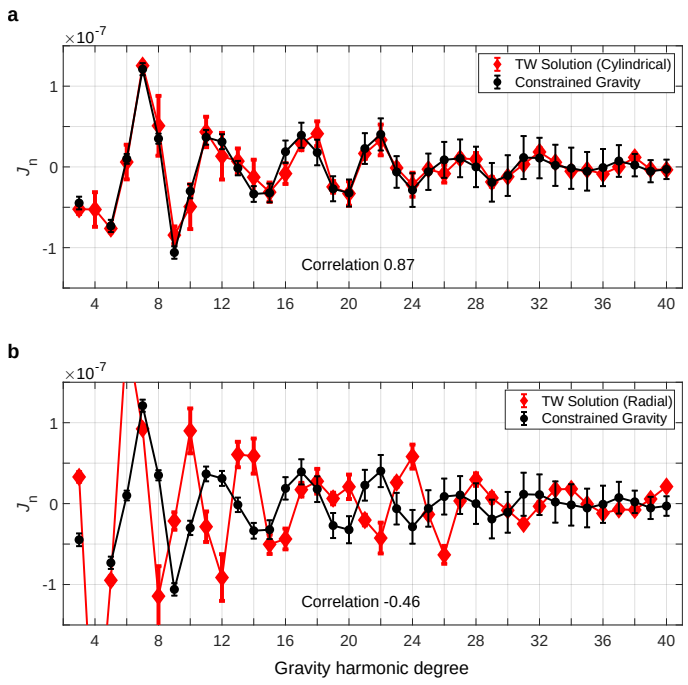

Figure 2: **Jupiter's gravity harmonics up to J_{40}.** The measured gravity harmonics with the constrained solution (black) and the corresponding calculated wind-induced gravity harmonics based on projecting the cloud-level winds inward (red) cylindrically along the direction of the spin axis (a), and radially (b). In both (a) and (b) the wind decays with a radial profile $Q(r)$ (see Methods, M2). For the measured even harmonics J_6, J_8 and J_{10} we subtract the non-dynamical values (ED Table 2) coming from internal structure models[12]. J_2 and J_4 were omitted because the relative contribution of the dynamics is very small[12]. The uncertainty in the measurements (black bars) is the 3σ uncertainty (i.e., 3 times the values given in Table 1), and for calculated dynamical uncertainty values come the uncertainty in the measured cloud-level winds[20] as shown in the gray envelope in ED Fig. 2.

when extending the cloud-level winds inwards radially instead of along the spin axis, showing that the high correlation up to J_{40} in Fig. 2a breaks when the flow is not aligned with the spin axis. In both cases presented here the decay of the flow amplitude inward is radial assuming the decay is related to higher pressure, either directly through the denser fluid[3] or due to the magnetic field[40,14]. However, since the exact vertical decay mechanism is unknown we also explore a possibility that the winds extend inward cylindrically and the decay also has a cylindrical orientation (ED Fig. 3). This third option also correlates less to the measurements, yet correlates better than the pure radial extension with radial decay. We thus conclude that the best fit is when the extension is cylindrical but the wind magnitude decays at depth radially.

The source of the wavy gravity signal

Further evidence for the flow orientation can be gained by understanding the origin of the wavy pattern in the gravity signal shown in Fig. 2. To do so, we analyze below several simplified profiles of the cloud-level winds (see also Methods, M6 & M7). First, we examine a case where the winds at all latitudes are set to zero, and only the jet at 21°N is retained (Fig. 3a, blue). This produces a gravity signal that captures much of the measured signal (Fig. 3b, and see corresponding density anomaly in ED Fig. 4). To confirm that indeed this jet is setting the frequency of this wavy pattern, we experiment with the wind profile by again keeping only a single jet, but artificially shifting the 21°N equatorward by 5° so that a single jet exists at 16°N (Fig. 3a, red) and alternately shifting it poleward so that single jet exists at 26°N (Fig. 3a, green). The resulting gravity spectra (Fig. 3b) shows that none of these synthetic wind profiles match the data, with the poleward (equatorward) jet shift decreasing (increasing) the wave frequency. This implies that indeed the observed cloud-level winds, and particularly the 21°N jet, set the gravity spectrum. Despite the importance of the 21°N jet the rest of the winds between 25°S and 25°N do improve the match to observations (Fig. 3c, black), with most of the secondary contribution coming from the 18°S jet. We further demonstrate this when examining the surface gravity (Fig. 4b).

The dominance of the 21°N jet serves as evidence that the flows extend inward cylindrically. This can be understood by considering the three regions illustrated in Fig. 1b. In region 1, outward of the tangent cylinder (which encompasses a 3000 km depth at the equator), there are strong winds at the cloud-level, however, the winds do not penetrate deep when projected cylindrically, meaning there is little mass involved in this flow and thus little influence on the gravity harmonics. Therefore the equatorial winds (equatorward of latitude 17° where the tangent cylinder outcrops the surface), despite being strong, have a negligible contribution to the gravity signal. The integrated cylindrical mass around a latitude circle (Methods, M5), which peaks at latitude 17°, is shown in Fig. 1c. Poleward, in region 2, where there are the strong jets at 21°N and 18°S, the winds are both strong and penetrate deep (Fig. 1c) over a region with significant mass (with a large mass anomaly across the jets, Fig. 1d), and thus contribute strongly to the gravity signal. Previous studies, varying the winds in latitude[41], or using barotropic winds[42], also demonstrated the

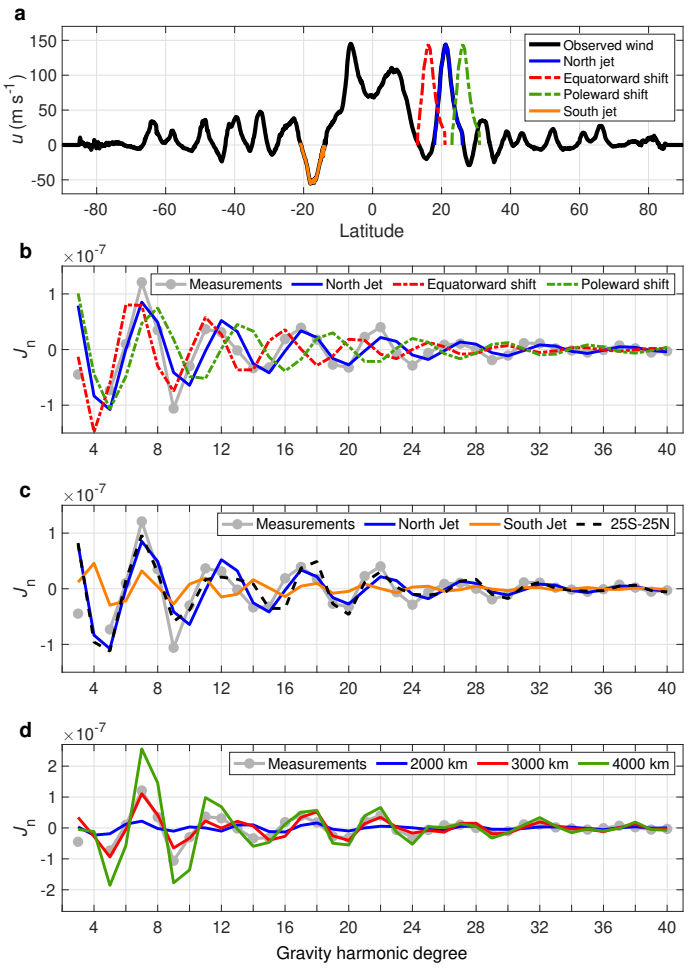

Figure 3: **The specific jets controlling the structure of the gravity harmonic pattern. a.** Jupiter's cloud-level winds[20] with the 21°N jet highlighted (blue) and the experimental equatorward and poleward shifts to it illustrated in the dash-dot red and green, respectively. Also highlighted is the 18°S jet (orange). **b.** wind-induced gravity harmonics ($J_2 - J_{40}$) resulting just from the 21°N jet (blue), a similar jet perturbed equatorward (red) and a similar jet perturbed poleward (green) compared to the measurements shown in Fig. 2 (gray). The error bars for the measurements are shown in Fig. 2 (black) and emitted here for clarity. **c.** The separate contributions of the 21°N jet (blue), 18°S jet (orange) and full 25°S-25°N region (dashed black). **d.** The gravity harmonics from the full winds (as in Fig. 2a), considering different decay depths, with the flow decaying to 2% of the surface value at 2000 km (blue), 3000 km (red) and 4000 km (green), (see ED Fig. 2 for radial decay profiles).

importance of region 2. Note that the jet at 21°N is ~ 3 times stronger than the jet at 18°S and just slightly less aligned with the region of maximum mass (Fig. 1c), and thus contributes about twice as much to the gravity signal (Fig. 1d). In region 3, poleward of these strong jets, the jets are weaker and involve less mass going poleward (Fig. 1c), and thus the contribution to the gravity is small. Note that if the flow would have projected inward radially (Fig. 2b), the equatorial flows (region 1) would have contributed much more to the gravity signal, and the contribution of region 2 would not have been so dominant. The dominance of the 21°N jet in the gravity harmonics (Fig. 3b) serves thus as direct observational evidence that the flows project inward cylindrically.

Fig. 3b shows clearly that the frequency and decay of the wavy pattern of the gravity signal come mainly from the 21°N jet. The frequency of the wave pattern emerges from the location of the most dominant jet. We illustrate this in ED Fig. 5 and ED Fig. 6 using a simple pulse (section M6), and demonstrate this even analytically (in the limit of high harmonics) in section M7, where an analytic expression gives the relation between the gravity anomaly location and the wave frequency. The decay of the wave (i.e., half the amplitude at $\sim$ harmonic 20) is set by the width of the jet (gravity pulse), where the narrower the jet the longer it takes the signal to decay. The amplitude of this signal comes from the wind penetration depth, as deeper regions are denser and the gravity signal is thus stronger. This is demonstrated in Fig. 3d, showing the gravity signal resulting from the full winds (Fig. 3a, black), projected inward along the direction of the spin axis and decaying radially with a fixed hyperbolic tangent function to different depths (ED Fig. 2). In this analysis, we do not optimize the decay function to allow proper comparison between the solutions. It is evident that the winds decaying to 3000 km match best the measured gravity harmonics as shown previously[10]. Interestingly, as the frequency and decay of the wave do not depend on depth, some of the gravity harmonics, which happen to be at the zero crossing of the wave, do not depend on depth. Particularly, the wind induced J_6, which is crucial for interior structure models[43,44,45], happens to be very close to zero, and thus contributes very little to the overall J_6. This can be potentially used to put stronger constraints on the dynamical J_n used in interior models.

Analysis of the surface gravity at cloud-level

Taking a different approach to examining the gravity harmonics, the analysis can be done on the surface gravity itself. Fig. 4a shows the surface gravity as function of latitude, taking into account only the first four odd harmonics (the low-order harmonics resulting purely from the dynamics). As expected, there is a match between the measured data from the previous analysis, the new gravity analysis, and the calculated wind-induced gravity harmonics. In Fig. 4b we extend the analysis to include all purely dynamical harmonics up to J_N (where $N = 40$, except the early Juno study (blue) where N was 24 and the mid-mission update (green) where N was 30, see Methods, M3). The results show that even though the high gravity harmonics of the early analyses[9,29] are very different from the new gravity analysis (ED Fig. 1), their combination is very similar between 40°S and 40°N when mapped to the surface gravity, indicating the small scale variability of Jupiter's gravity field is resolved in the previous analyses in this region. The constrained gravity solution (black) matches the full zonal wind-induced profile (red) at high-latitudes as well. Setting constraints at high latitudes effectively decorrelates the individual contributions and allows estimating the harmonics beyond J_{10}. In the absence of those constraints, the estimation errors of surface gravity in the polar regions are large as a consequence of the inability to estimate the high degree harmonics. For this reason, the gravity solutions in the polar regions[9,29], although ap-

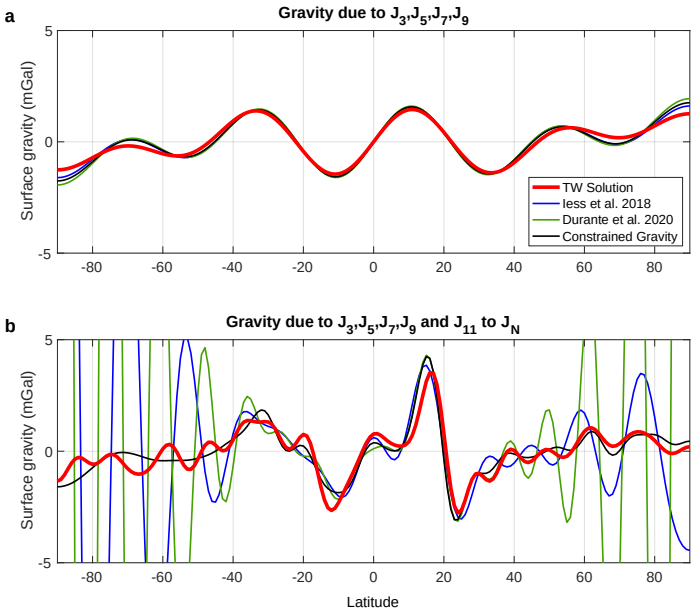

Figure 4: **The wind induced surface gravity. a.** Jupiter's surface gravity based on the low-degree purely dynamic gravity harmonics (J_3, J_5, J_7 and J_9), using the measurements from the first two gravity orbits[9] (blue), the first 10 gravity orbits[29] (green), the calculated harmonics based on the cloud-level winds using thermal wind balance (red) and the constrained solution presented in this study (black). **b.** The same, but using all dynamical harmonics (J_3, J_5, J_7, J_9 and $J_{11} - J_N$, see Methods, M3).

parently very different in Fig. 4b, are statistically identical. Note also that in addition to the strong signal due tho the 21°N jet, the signal due to the opposing southern hemisphere jet is also evident.

Discussion

This study presents the gravity harmonics of Jupiter to high-degree following Juno's multiple flybys of Jupiter, taking into account that the dynamical contribution at high latitudes is small. This new analysis enables resolving several key issues regarding the uniqueness and dynamical balances of the flow field of Jupiter. Deducing the flow field from the gravity spectrum is by definition non-unique, since the flow field has endless degrees of freedom, and many different flow fields can match a finite number of gravity harmonics. In addition, the gravity is an integrated measure of the mass and thus the non-uniqueness in inherent. Given this, the uniqueness question has been debated greatly in the literature[46,10,47], and other flow fields completely unrelated to the cloud-level winds have been suggested[47], and shown to be able to match J_3, J_5, J_7, and J_9. However, the match of the gravity signal from the cloud-level winds projected inward up to J_{40}, and the dynamical explanation of the wavy pattern serve as strong evidence that the gravity signal comes from the cloud-level flows. In addition, this study shows that higher order corrections to thermal-wind balance, which have been argued to be necessary for the gravity analysis[48,49], can be neglected (ED Fig. 7) as this analysis using thermal-wind balance to relate the flow and the density anomalies[48,50,51], gives a gravity field that correlates very well to the measurements. The same wavy pattern of the signal also explains the signs of the low-degree harmonics J_3, J_5, J_7, and J_9, which have been measured early in the Juno mission[9].

Overall, these results confirm that indeed the cloud-level winds imprint the gravity signal, and provide direct evidence to the cylindrical structure of the flows, which penetrate cylindrically down to $\sim 10^5$ bar (3000 km). The cylindrical orientation also implies that the flows are nearly barotropic (via the Taylor-Proudman theorem[31]), particularly in the upper levels, as indicated by the best matching zonal wind vertical profiles (ED Fig. 2). The 3000 km depth of the zonal flows, as well as the equivalent 9000 km depth found on Saturn[52,14], fit well the depth at which electrical conductivity rises on both planets[13], hinting to the connection between the decay of the flow and the magnetic field[40]. Yet, there is currently no complete mechanism that can quantitatively explain the decay of the flow with depth, and other mechanisms involving compressibility[3] or a stable layer[17,53] have been suggested as well. This paper provides observational evidence for the structure of the flow at depth and the next challenge is to mechanistically explain this structure.

References

1. Vasavada, A. R. & Showman, A. P. Jovian atmospheric dynamics: An update after Galileo and Cassini. *Reports of Progress in Physics* **68**, 1935–1996 (2005).
2. Duer, K. *et al.* Evidence for multiple Ferrel-like cells on Jupiter. *Geophys. Res. Lett.* **48** (2021).
3. Kaspi, Y., Flierl, G. R. & Showman, A. P. The deep wind structure of the giant planets: Results from an anelastic general circulation model. *Icarus* **202**, 525–542 (2009).
4. Adriani, A. *et al.* Clusters of cyclones encircling Jupiter's poles. *Nature* **555**, 216–219 (2018).
5. Gavriel, N. & Kaspi, Y. The number and location of Jupiter's circumpolar cyclones explained by vorticity dynamics. *Nature Geoscience* **14**, 559–563 (2021).
6. Bolton, S. J. *et al.* Jupiter's interior and deep atmosphere: The initial pole-to-pole passes with the Juno spacecraft. *Science* **356**, 821–825 (2017).
7. Stevenson, D. J. Jupiter's interior as revealed by Juno. *Ann. Rev. Earth Plan. Sci.* **48**, 465–489 (2020).
8. Bolton, S. J. *et al.* Microwave observations reveal the deep extent and structure of Jupiter's atmospheric vortices. *Science* **374**, 968–972 (2021).
9. Iess, L. *et al.* Measurement of Jupiter's asymmetric gravity field. *Nature* **555**, 220–222 (2018).
10. Kaspi, Y. *et al.* Jupiter's atmospheric jet streams extend thousands of kilometres deep. *Nature* **555**, 223–226 (2018).
11. Kaspi, Y. Inferring the depth of the zonal jets on Jupiter and Saturn from odd gravity harmonics. *Geophys. Res. Lett.* **40**, 676–680 (2013).
12. Guillot, T. *et al.* A suppression of differential rotation in Jupiter's deep interior. *Nature* **555**, 227–230 (2018).
13. Kaspi, Y. *et al.* Comparison of the deep atmospheric dynamics of Jupiter and Saturn in light of the Juno and Cassini gravity measurements. *Space Sci. Rev.* **216**, 84 (2020).
14. Galanti, E. & Kaspi, Y. Combined magnetic and gravity measurements probe the deep zonal flows of the gas giants. *Mon. Not. Roy. Astro. Soc.* **501**, 2352–2362 (2021).
15. Moore, K. M. *et al.* Time variation of Jupiter's internal magnetic field consistent with zonal wind advection. *Nature Astronomy* **3**, 730–735 (2019).
16. Bloxham, J. *et al.* Differential rotation in Jupiter's interior revealed by simultaneous inversion for the magnetic field and zonal flux velocity. *J. Geophys. Res. (Planets)* **127**, e07138 (2022).

17. Christensen, U. R., Wicht, J. & Dietrich, W. Mechanisms for limiting the depth of zonal winds in the gas giant planets. *Astrophys. J.* **890**, 61 (2020).
18. Busse, F. H. A simple model of convection in the Jovian atmosphere. *Icarus* **29**, 255–260 (1976).
19. Christensen, U. R. Zonal flow driven by deep convection in the major planets. *Geophys. Res. Lett.* **28**, 2553–2556 (2001).
20. Tollefson, J. *et al.* Changes in Jupiter's zonal wind profile preceding and during the Juno mission. *Icarus* **296**, 163–178 (2017).
21. Guillot, T. Interiors of giant planets inside and outside the solar system. *Science* **286**, 72–77 (1999).
22. Wahl, S. *et al.* Comparing Jupiter interior structure models to Juno gravity measurements and the role of an expanded core. *Geophys. Res. Lett.* **44**, 4649–4659 (2017).
23. Folkner, W., Iess, L., Tortora, P. & more. Jupiter gravity field from first two orbits by Juno. *Geophys. Res. Lett.* **44**, 4694–4700 (2017).
24. Kaspi, Y., Hubbard, W. B., Showman, A. P. & Flierl, G. R. Gravitational signature of Jupiter's internal dynamics. *Geophys. Res. Lett.* **37**, L01204 (2010).
25. Hubbard, W. B. Note: Gravitational signature of Jupiter's deep zonal flows. *Icarus* **137**, 357–359 (1999).
26. Grassi, D. *et al.* First estimate of wind fields in the Jupiter polar regions from JIRAM-Juno images. *J. Geophys. Res. (Planets)* **123**, 1511–1524 (2018).
27. Konopliv, A. S., Park, R. S. & Ermakov, A. I. The mercury gravity field, orientation, love number, and ephemeris from the MESSENGER radiometric tracking data. *Icarus* **335**, 113386 (2020).
28. Park, R. S. *et al.* Evidence of non-uniform crust of Ceres from Dawn's high-resolution gravity data. *Nature Astronomy* **4**, 748–755 (2020).
29. Durante, D. *et al.* Jupiter's gravity field halfway through the Juno mission. *Geophys. Res. Lett.* **47** (2020).
30. Galanti, E. & Kaspi, Y. An adjoint based method for the inversion of the Juno and Cassini gravity measurements into wind fields. *Astrophys. J.* **820**, 91 (2016).
31. Pedlosky, J. *Geophysical Fluid Dynamics* (pp. 710. Springer-Verlag, 1987).
32. Zhang, K. Spiralling columnar convection in rapidly rotating spherical fluid shells. *J. Fluid Mech.* **236**, 535–556 (1992).
33. Busse, F. H. & Carrigan, C. R. Laboratory simulation of thermal convection in rotating planets and stars. *Science* **191**, 81–83 (1976).
34. Heimpel, M., Aurnou, J. & Wicht, J. Simulation of equatorial and high-latitude jets on Jupiter in a deep convection model. *Nature* **438**, 193–196 (2005).
35. Gastine, T. & Wicht, J. Effects of compressibility on driving zonal flow in gas giants. *Icarus* **219**, 428–442 (2012).
36. Heimpel, M., Gastine, T. & Wicht, J. Simulation of deep-seated zonal jets and shallow vortices in gas giant atmospheres. *Nature Geoscience* **9**, 19–23 (2016).
37. Liu, J. & Schneider, T. Mechanisms of jet formation on the giant planets. *J. Atmos. Sci.* **67**, 3652–3672 (2010).
38. Cao, H. & Stevenson, D. J. Gravity and zonal flows of giant planets: From the Euler equation to the thermal wind equation. *J. Geophys. Res. (Planets)* **122**, 686–700 (2017).
39. Duer, K., Galanti, E. & Kaspi, Y. The range of Jupiter's flow structures fitting the Juno asymmetric gravity measurements. *J. Geophys. Res. (Planets)* **125**, e2019JE006 (2020).
40. Liu, J., Goldreich, P. M. & Stevenson, D. J. Constraints on deep-seated zonal winds inside Jupiter and Saturn. *Icarus* **196**, 653–664 (2008).
41. Galanti, E. *et al.* Constraints on the latitudinal profile of Jupiter's deep jets. *Geophys. Res. Lett.* **48**, e92912 (2021).
42. Kulowski, L., Cao, H., Yadav, R. K. & Bloxham, J. Investigating barotropic zonal flow in Jupiter's deep atmosphere using Juno gravitational data. *J. Geophys. Res. (Planets)* **126**, e06795 (2021).
43. Debras, F. & Chabrier, G. New models of Jupiter in the context of Juno and Galileo. *Astrophys. J.* **872**, 100– (2019).
44. Militzer, B. *et al.* Juno spacecraft measurements of Jupiter's gravity imply a dilute core. *Planet. Sci. J.* **3**, 185 (2022).
45. Miguel, Y. *et al.* Jupiter's inhomogeneous envelope. *Astron. and Astrophys.* **662**, A18 (2022).
46. Galanti, E. & Kaspi, Y. Deciphering Jupiters deep flow dynamics using the upcoming Juno gravity measurements and an adjoint based dynamical model. *Icarus* **286**, 46–55 (2017).
47. Kong, D., Zhang, K., Schubert, G. & Anderson, J. D. Origin of Jupiter's cloud-level zonal winds remains a puzzle even after Juno. *Proc. Natl. Acad. Sci. U.S.A.* **115**, 8499–8504 (2018).
48. Zhang, K., Kong, D. & Schubert, G. Thermal-gravitational wind equation for the wind-induced gravitational signature of giant gaseous planets: Mathematical derivation, numerical method and illustrative solutions. *Astrophys. J.* **806**, 270–279 (2015).
49. Wicht, J., Dietrich, W., Wulff, P. & Christensen, U. R. Linking zonal winds and gravity: the relative importance of dynamic self-gravity. *Mon. Not. Roy. Astro. Soc.* **492**, 3364–3374 (2020).
50. Kaspi, Y., Davighi, J. E., Galanti, E. & Hubbard, W. B. The gravitational signature of internal flows in giant planets: comparing the thermal wind approach with barotropic potential-surface methods. *Icarus* **276**, 170–181 (2016).
51. Galanti, E., Kaspi, Y. & Tziperman, E. A full, self-consistent, treatment of thermal wind balance on fluid planets. *J. Fluid Mech.* **810**, 175–195 (2017).
52. Iess, L. *et al.* Measurement and implications of Saturn's gravity field and ring mass. *Science* **364**, 1052– (2019).
53. Gastine, T. & Wicht, J. Stable stratification promotes multiple zonal jets in a turbulent Jovian dynamo model. *Icarus* **368**, 114514 (2021).
54. Park, R. S. *et al.* A partially differentiated interior for Ceres deduced from its gravity field and shape. *Nature* **537**, 515–517 (2016).
55. Park, R. S., Folkner, W. M., Williams, J. G. & Boggs, D. H. The JPL planetary and lunar ephemerides DE440 and DE441. *Astronom. J.* **161**, 105 (2021).
56. Park, R. S. *et al.* Precession of Mercury's perihelion from ranging to the MESSENGER spacecraft. *Astronom. J.* **153** (2017).
57. Wicht, J., Gastine, T. & Duarte, L. D. V. Dynamo action in the steeply decaying conductivity region of Jupiter-like dynamo models. *J. Geophys. Res. (Planets)* **124**, 837–863 (2019).

Acknowledgments

We thank Rei Chemke for helpful discussions. We thank the four reviewers for their insightful comments and improving this work. Particularly, we thank one of the reviewers for suggesting the analytical analysis presented in section M7. Y.K, E.G, K.D. and N.G. acknowledge support from the Israeli Ministry of Science and Technology (grant 96958) and the Helen Kimmel Center for Planetary Science at the Weizmann Institute. D.D and L.I. acknowledge support from the Italian Space Agency (grant 2022-16-HH.0). All authors acknowledge support from the Juno mission.

Data availability

All data is available at: https://dataverse.harvard.edu/dataset.xhtml?persisten

Author contributions

Y.K. and E.G. designed the study. Y.K. wrote the paper. E.G. developed the gravity inversion model and performed the calculations. R.S.P designed the constrained approach and carried out the analysis of Juno gravity data with D.B, M.P, D.D. and L.I.. K.D. and N.G performed the idealized models interpreting the gravity signal, density structure and ring mass. D.J.S. led the working group within the Juno Science Team and provided theoretical support. T.G. provided theoretical support. S.J.B. supervised the planning, execution, and definition of the Juno gravity

experiment and provided theoretical support. All authors contributed to the discussion and interpretation of the results.

Methods

M1. Analysis of the Juno radio Doppler measurements

This study is based on gravity data collected from a total of 26 perijove data, where 19 arcs have the two-way dual frequency (X and Ka band) data[54,29]. The acquisition of the first perijove data started on August 27, 2016 (i.e., perijove 1) and the last data considered in this study ended on October 17, 2021 (i.e., perijove 37). To recover Jupiter's gravity field, the external gravitational potential of Jupiter can be modeled using a spherical harmonic expansion:

$$\Phi(r,\theta,\phi) = \frac{GM}{r}\sum_{n=0}^{\infty}\sum_{m=0}^{n}\left(\frac{R_e}{r}\right)^n P_{n,m}(\sin\theta)\times \left[C_{n,m}\cos(m\phi)+S_{n,m}\sin(m\phi)\right], \quad (1)$$

where G is the universal gravitational constant, M is the mass of Jupiter, R_e is the reference equatorial radius of Jupiter (71,492 km), $P_{n,m}$ are the associated Legendre functions, and $C_{n,m}$ and ,S_{nm} are the unnormalized spherical harmonic coefficients (the corresponding unnormalized zonal harmonics are $J_n = -C_{n,0}$). The gravitational acceleration of an external point source (e.g., Juno spacecraft), defined by the latitude (θ), longitude (ϕ), and radius (r), is given by the gradient of this potential. In this study, the gravity field of Jupiter is modeled with a degree 40 zonal field (i.e., $J_2 - J_{40}$) plus four tesseral degree 2 terms (i.e., $C_{2,1}$, $S_{2,1}$, $C_{2,2}$ and $S_{2,2}$). For planetary motion, JPL's DE440 planetary and lunar ephemerides is used[55]. Other globally estimated parameters are Jupiter's spin-pole motion, and tidal Love numbers. For each perijove, locally estimated parameters are the spacecraft state, solar pressure scaled factor, and a correction to the first degree 12 zonal coefficients.

Juno's orbit is highly inclined relative to Jupiter's equator ($\sim 90^\circ - 106^\circ$) and the periapsis latitude varies from 3.78° to 30.65°. The unconstrained global solution has a sensitivity of up to $\sim J_{12}$ since Juno data sensitivity is saturated near the poles (i.e., far from Jupiter when the Juno spacecraft is tracked by NASA's Deep Space Network). Thus, a spatial constraint method often used for a sparse dataset was applied to extract shorter wavelength signatures[27,28]. For latitudes between (90°S, 40°S) and (70°N, 90°N), longitude and latitude grids were created for every two degrees, which would be equivalent to having latitude-only constraints scaled by $\sqrt{360^\circ/2^\circ} \sim 13$. For each grid point, the a priori surface acceleration value was constrained to be zero for zonal harmonics $J_{13} - J_{40}$, with empirically varying determined a priori uncertainties to reach a mapped a priori surface acceleration uncertainty of 1 mGal. Specifically, for each grid point, the a priori uncertainty was assumed to be 0.04 mGal, 0.1 mGal, 0.2 mGal, 0.3 mGal, 0.4 mGal, 0.1 mGal, and 0.04 mGal for latitude bands of (90°S, 80°S), (80°S, 70°S), (70°S, 60°S), (60°S, 50°S), (50°S, 40°S), (70°N, 80°N), (80°N, 90N). With this constraint, the recovered zonal coefficients, $J_2 - J_{12}$, would represent Jupiter's global zonal field, whereas the recovered $J_{13} - J_{40}$ would be a localized solution. In other words, this constraint method extracts the zonal harmonics $J_{13} - J_{40}$ mainly from the latitude band (40°S, 70°N). This constraint technique is similar to the Kaula constraint[27,54,28], but uses a spatial constraint instead of a spectrum constraint. The recovered Jupiter zonal gravity field is shown in ED Table 1. Fig. 4 shows that the surface gravity from high-degree harmonics resulting from the estimation of the constrained harmonics $J_{13} - J_{40}$ is about 1 mGal, which is the expected range for gravity anomalies in the polar regions

Since we are working with a sparse dataset, it is crucial to assess the robustness of the recovered zonal coefficients. One method that is often used for assessing the validity of the estimated values is testing the repeatability of the solution using subsets of data[56]. We have tried estimating the zonal harmonics, $J_2 - J_{40}$, using various subsets of data, such as first half flybys, second half flybys, every other flybys, and flybys with only dual-frequency data. The final reported uncertainties in ED Table 1 are computed by scaling the formal uncertainties of $J_{13} - J_{40}$ by a factor of $1-2$ so that the differences of the subset solutions are bounded by the reported uncertainties. Thus, the recovered zonal harmonics and associated uncertainties are statistically valid and robust for the dynamical and measurement models we have used in our estimation process. We note that Fig. 2 shows 3 times these scaled uncertainties reported in ED Table 1 such that the error bars show a more conservative representation of estimated uncertainties. Even in this conservative case, zonal harmonics up to J_{24} are clearly recovered, and the wavy pattern we explain physically (see Methods, M6) extends through J_{40}, giving confidence that these high harmonics have a physical meaning even when close to the formal uncertainty.

M2. The vertical wind profile

In this study we examine three different scenarios defining how the wind is expected to be organized below the observed cloud-level wind. In the first scenario, the interior wind is organized in columns reflecting the cloud-level winds,

$$u^{\rm proj}(r,\theta) = u^{\rm obs}(\theta'), \quad (2)$$

where $\theta' = \arccos(r\cos\theta/R_e)$ relates the latitude of the interior location θ, to the latitude at cloud level θ', which is at the same distance from the spin axis. This scenario is supported by many studies[18,19,34,35], as discussed in the main text, and is used in the calculation of all results, aside from those shown in Fig. 2b and ED Fig. 3 (see below). In Fig. 2b we examine the second scenario, in which the wind observed at the cloud level is projected inward in the radial direction, so that

$$u^{\rm proj}(r,\theta) = u^{\rm obs}(\theta). \quad (3)$$

This scenario reflects a hypothetical dynamical situation where the rotation of the planet does not play a role in the deep structure of the zonal flows.

Given the wind scenario, we then allow for these two cases the flow to decay in the radial direction, to give the out-coming flow

field

$$u(r,\theta) \quad = \quad u^{\rm proj}(r,\theta)Q(r), \tag{4}$$

where the radial decay function $Q(r)$ is defined as

$$Q(r) \quad = \quad (1-\alpha)\exp\left(-\frac{\Delta r}{H}\right)+\alpha\left[\frac{\tanh\left(-\frac{\Delta r-H}{\Delta H}\right)+1}{\tanh\left(\frac{H}{\Delta H}\right)+1}\right], \tag{5}$$

where $\Delta r = R_e - r$, H is the scale height, α is the contribution ratio between an exponential and a normalized hyperbolic tangent function, and ΔH is the width of the hyperbolic tangent[10]. This flow field is then used to calculate the gravity perturbation caused by the winds, as discussed below. The choice of the wind decay being radial is based on physical reasoning, since the pressure and density increase radially, resulting in suggested radial decay mechanisms due to compressibility[3], Ohmic dissipation[40] or a stable layer[17]. The values giving the best-fit (to J_3, J_5, J_7 and J_9) of the optimized vertical profile, used in Fig. 2 (ED Fig. 2b, black), are $H = 2,101$ km, $\Delta H = 842$ km, and $\alpha = 0.68$. For the cases where we compare the same profile at different depths (unoptimized in order for a proper comparison in Fig. 3d), the values are $\alpha = 1$, $\Delta H = 500$ km, and $H = 1000$ km, $H = 2000$ km, and $H = 3000$ km for the blue, red and green profiles, respectively. Note the quoted values in the legend of Fig. 3d and ED Fig. 2b are for where the flow decays to 2% of the surface flow and not the H value from Eq. 5. The values for the yellow curve, which includes the magnetic considerations are $H_M = 200$ km, $f_M = 0.55$ km, and $\delta H_T = 204$ km as discussed in a separate study[14]. This profile and the best-fitting zonal wind meridional profile[14] give similar gravity harmonics to those shown in Fig. 2a.

A third option we examine is that both the extension of the cloud-level winds and their decay are along the direction of the spin axis (ED Fig. 3). In this case, Δr in equation 5 is replaced by the cylindrical distance $z = R_e \sin\theta' - |r\sin\theta|$. The correlation in this case is lesser (0.41) than when the winds extend cylindrically and the decay is radial. In this case the best optimized case has $H = 3,990$ km, $\Delta H = 2,057$ km, and $\alpha = 0.9$ (ED Fig. 3c). For comparison, panel b has the same H, ΔH and α values as those of the original optimization shown in (ED Fig. 3a) and Fig. 2a. When the decay is cylindrical the maximum velocity is always at the outer levels of each cylinder (which is not necessarily the case in the radial decay case), which is a consideration to take into account when further investigating the decay mechanism[57,17].

M3. Calculating the wind-induced gravity harmonics and surface gravity

The gravity field, a measure of the planet mass distribution, depends also on the zonal winds via a balance between the anomalous density field and the flow field, as expected in large-scale flow on fast-rotating planets, such as Jupiter[24]. Here we give a short version of the derivation of this balance (for the full derivation refer to other studies[50,51,38,10]). The momentum balance, under the assumption of a small Rossby number (large scale motions on a fast rotating planet) and a steady state, is

$$2\Omega\times(\rho\mathbf{u}) \quad = \quad -\nabla p - \rho\mathbf{g} - \rho\Omega\times\Omega\times\mathbf{r}, \tag{6}$$

where $\mathbf{u}$ is the 3D flow vector, Ω is the planetary rotation rate, ρ is density, p is pressure and $\mathbf{g}$ is the gravitational acceleration[31]. Separating the solutions to a rigid body solution $\rho_s(r,\theta)$, $p_s(r,\theta)$, and $\mathbf{g}_s(r,\theta)$ in which $\mathbf{u} = 0$, and a deviation due to the dynamics $\rho'(r,\theta)$, $p'(r,\theta)$, and $\mathbf{g}'(r,\theta)$, the dynamical balance becomes

$$2\Omega\times(\rho_s\mathbf{u}) = \quad -\nabla p' - \rho_s\mathbf{g}' - \rho'\mathbf{g}_s - \rho'\Omega\times\Omega\times\mathbf{r}. \tag{7}$$

Next, neglecting all terms including g' and the centrifugal term, which are of lower order[51] (ED Fig. 7), assuming sphericity (with ρ_s, p_s and $\mathbf{g}_s$ becoming radial functions only), and taking the curl, results in the zonal component of (7) being

$$2\Omega r\frac{\partial}{\partial z}(\rho_s u) = g_s\frac{\partial\rho'}{\partial\theta}, \tag{8}$$

where z is the direction of the spin axis. Given a zonal flow field u, this equation can be solved for ρ' up to an integration constant $\rho_0(r)$ that does not affect the gravity harmonics[50,10]. The wind-induced gravity harmonics are calculated as the volume integral of ρ' projected onto Legendre polynomials

$$\Delta J_n = \frac{2\pi}{MR_e^n}\int_0^{R_e} r^{n+2}dr \int_{\theta=-\pi/2}^{\pi/2} P_n(\sin\theta)\,\rho'(r,\theta)\cos\theta\, d\theta. \tag{9}$$

The calculated odd gravity harmonics $n = 3,5,7,9$ are then compared to the measured values, and an optimal solution for the flow field is found by varying the parameters H,α and ΔH, using the adjoint method of optimization[30]. Note the $(r/R_e)^n$ factor in (9) results in the higher harmonics being smaller, but since this factor for the relevant depths (up to 3000 km) is close to unity these variations are not large.

The gravity harmonics can be used to calculate the surface gravity anomaly in the radial direction, via

$$\Delta g_r(\theta) \quad = \quad -\frac{GM}{R_e^2}\sum_n (n+1)\,\Delta J_n P_n(\sin\theta), \tag{10}$$

with $n = 3,5,7,9$ used in Fig. 4a. In Fig. 4b, in addition to $n = 3,5,7,9$, we included also the high harmonics used in each of the earlier gravity analyses ($J_{11} - J_N$), i.e., harmonics $11-24$ for the first 2018 Juno study[9], harmonics $11-30$ for updated 2020 Juno study[29], and harmonics $11-40$ for the new gravity analysis and the thermal-wind solution.

It has been shown that while the term including g' in (7) is small, it can still give a contribution to the low order gravity harmonics of the order of several tens of percent[48,51,49]. In order to estimate this contribution, we adopted the method of Wicht et al., 2020[49] and calculate the gravity harmonics when including the g' term (dynamic self-gravity). The solutions presented in ED Fig. 7, which are consistent with Wicht et al., 2020, confirm that these contributions are small.

M4. The wind induced density anomalies and gravity signal

To better understand the relation between the wind field and the density anomaly structure (Eq. 8), and the relation between the density anomalies and the detected radial gravity signal at the cloud-level presented in Fig. 4 (Δg_r, Eq. 10), we examine the three fields together with the wind decay rate, ($Q(r)$, Eq. 4,5) and the static density component (ED Fig. 4). For a clear comparison and to allow better understanding of the density anomalies, we present the case of the full wind field (ED Fig. 4b) together with a synthetic case with the 21°N jet wind field alone (ED Fig. 4c), as a significant part of the gravity signal comes directly from it (Fig. 3). The wind field is composed by projecting the cloud-level-wind in a direction parallel to the axis of rotation ($u^{\mathrm{proj}}(\theta,r)$, Eq. 4) and multiplying it by the best-fit radial decay function ($Q(r)$, ED Fig. 4a), representing the fraction of the cloud-level wind at every depth. Note that as u^{proj} has no inhibited decay, its vertical derivative $(\partial/\partial z)$ is equal to zero. For the examples presented here, the 3000 km depth level represents the depth where the wind decays to about 20% of its original velocity, and it is the decay rate inflection point (ED Fig. 4g).

The dynamical density resulting from a wind field is calculated using TW balance, Eq. 8. For determining the absolute dynamical density, the integration constant is set to zero[50], exemplified in a transition from negative to positive anomalies in the meridional direction (ED Fig. 4e,f), which sums to zero at each depth. Note that this choice does not affect the results as this radial integration constant does not project on the J_n, which are only a function of latitude[50].

It is notable that when the wind field is composed of a single jet (ED Fig. 4c), the resulting dynamical density has a single latitudinal jump (ED Fig. 4f), matching the jet location. This helps clarify the more complicated dynamical density of the full wind (ED Fig. 4e), where each latitudinal shear matches exactly the location of a jet-stream (ED Fig. 4b). In the vertical direction, there appears a clear transition in the depth of 1900 km (black dashed lines, ED Fig. 4). This depth is the transitioning point between two competing factors, the vertical change in the static density (ρ_s) and the vertical change in the wind decay rate. We can simplify the left-hand side of Eq. 8 by recalling that the derivative along the direction of the spin axis of u^{proj} is zero and open the derivative, such that

$$2\Omega r\frac{\partial(\rho_s u)}{\partial z}=2\Omega r u^{\mathrm{proj}}\frac{\partial(Q\rho_s)}{\partial z}=2\Omega r u^{\mathrm{proj}}\left[Q\frac{\partial\rho_s}{\partial z}+\rho_s\frac{\partial Q}{\partial z}\right]. \tag{11}$$

In relatively shallow depths, the static density increases by several orders of magnitude (ED Fig. 4d), making its shear $(\partial\bar{\rho}/\partial z)$ positive and dominant (ED Fig. 4g, orange). However, deeper than 1900 km, the wind decay shear $(\partial Q/\partial z)$, which is negative, becomes dominant (ED Fig. 4g, yellow), flipping the sign of the shear in Eq. 11 resulting in the flip of sign of the dynamical density.

The radial gravity anomaly at the planet's surface that results from the wind-induced dynamical densities is a summation of the different considered gravitational harmonics and their associated Legendre polynomials. As a single jump in the dynamical density field will contribute to all the gravity harmonics (see main text), similar to a pulse that is represented in the spectral domain (ED Fig. 5), the gravitational harmonics resulting from the 21°N jet wind field are summed to give a gravity anomaly that varies with latitude (ED Fig. 4i). This gravity anomaly represents a large fraction of the full wind gravity anomaly (ED Fig. 4h) as it captures its overall magnitude and some latitudinal variations. This relates to Fig. 1, which intuitively shows that the 21°N jet (or region 2), being strong and comprising a significant mass fraction due to its location, causes a significant part of the gravitational anomaly detected by the spacecraft.

M5. Calculation of the ring mass

In Fig. 1c, the orange curve represents an estimation for the ring mass (M_{C}), projected inward parallel to the axis of rotation under each latitude, that moves like the projected cloud-level wind. To calculate this mass, we define a coordinate, z, which is the depth coordinate projected downward from the cloud level in a direction parallel to the axis of rotation. The radial depth can be calculated as

$$r(\theta,z)=\sqrt{R_J^2+z^2-2zR_J\sin\theta}, \tag{12}$$

where R_J $(=69{,}911$ km) is the mean radius of Jupiter. The column height, defined as the distance parallel to the axis of rotation from each point down to the equatorial plane, is $H_{\mathrm{C}}=R_{\mathrm{J}}\sin\theta$. The column mass is defined as

$$\int_0^{H_{\mathrm{C}}}\rho_s\,dz, \tag{13}$$

where $\rho_s(r)$ is the mean density[12]. To only include the mass fraction that participates in the motion of the cloud-level wind, we also consider the wind decay function[10], $Q(r)$, such that the wind-participating cylindrical ring mass is

$$M_{\mathrm{C}}=2\pi R_{\mathrm{J}}\cos(\theta)\int_0^{H_{\mathrm{C}}}\rho_s Q\,dz. \tag{14}$$

M6. The source for the waviness in the wind-induced gravity harmonics

In order to give physical intuition to the wavy nature of the gravity harmonics we perform a synthetic analysis of a pulse in a real space, and decompose it using the discrete Fourier transform (ED Fig. 5). For simplicity, we decompose a 1D signal in spectral space and show that the results are robust and give the right intuition for decomposing the gravity anomaly to gravity harmonics using Legendre polynomials on a sphere (ED Fig. 6). The pulse is defined as a Gaussian centered around location x_0, with an amplitude A and a width W, such that

$$y(x)=A\exp\left(-\frac{1}{2}\left(\frac{x-x_0}{W}\right)^2\right). \tag{15}$$

Hence, the three factors that define the pulse are its location (x_0), its height (A), and its width (W). We examine how each of these factors affects the representation of the pulse in the spectral space. It is well-known that the spectral representation of a pulse will include a wavy pattern of different frequencies. The pulse height (ED Fig. 5a), will intuitively dictate the amplitude of the wave (ED Fig. 5d), which can be nicely represented in a magnitude plot of the 30 lowest frequencies (ED Fig. 5g). A pulse with infinitesimal width will be represented in the spectral space by a 'perfect' wave, such that all wavenumbers contribute equally. This can be shown for a very narrow pulse width (ED Fig. 5b, blue), where the 'decay' of the frequencies vanishes (ED Fig. 5e,h, blue). However, a wide pulse (ED Fig. 5b, orange) requires fewer wavenumbers (ED Fig. 5e,h, orange), moving the cutoff such that the decay of frequencies is faster. Lastly, a pulse located at the middle of the domain (ED Fig. 5c, yellow) results in a very short wavelength (distance between neighboring peaks) in the spectral space representation (ED Fig. 5f,i, yellow). Pushing the pulse to the north increases the wavelength creating a 'smoother' wavy pattern.

We perform a second synthetic analysis of a hypothetical localized gravity anomaly (ED Fig. 6). We start with a gaussian function with a width of 5° (red line), centered around 16°N, which resembles in character the surface gravity resulting from the observed 21°N jet (ED Fig. 6a, gray line). Note that the surface gravity is composed from all the gravity harmonics $J_2 - J_{40}$. The resulting gravity signal (ED Fig. 6b) shows a wavy pattern, similar to that resulting from the observed wind profiles and which depends on the exact shape of the synthetic surface gravity. A narrower surface gravity signal (2° in width, ED Fig. 6a, blue) results in a wavy pattern that has less variation in the harmonics' amplitude, while a wider surface gravity signal (8° in width, ED Fig. 6a, green) does not change the lower harmonics, but makes the higher harmonics smaller, leading to a stronger 'decay'. In both cases, there is no effect on the frequency of the wave. This is equivalent to the simple case of changing the pulse width in spectral space. Moving the surface gravity signal in latitude (ED Fig. 6, lower panels), affects the frequency, similar to changing the pulse's location in the simple test above. An equatorward shift (5° in latitude, ED Fig. 6b, blue), increases the frequency, while a similar poleward shift results in a decreased frequency (ED Fig. 6b, green). The fact that the wavy pattern is not 'jumping' in sign between gravity harmonics suggests that the pulse responsible for this signal is off-equatorial, as shown in the simple case above of a centered pulse. Moreover, a pulse that will be close to the pole will create a much 'smoother' wave, hence, the jet location is not surprising due to the specific wavelength of the gravity harmonics. It is also evident that shifting the surface gravity signal does not change the amplitude of the wavy patten in the gravity harmonics, neither for the lower or higher harmonics. The amplitude analogy is presented in the main text (Fig. 3d), where the different decay depths will generate different amplitude in the surface gravity signal.

We conclude that zonal jet at 21°N has a localized positive expression in the surface gravity (see also ED Fig. 4), and that the signal, when decomposed into the Legendre polynomials, has a wavy expression in the gravity harmonics. This is completely equivalent to a much simpler case of a pulse decomposed using a Fourier transform. The frequency of the wavy pattern is set by the latitude of the surface gravity (resulting from the location of the jet), the amplitude of the wave is set by the decay structure and hence the amplitude of the surface gravity signal, and how the wavy pattern decays with higher harmonics, is set by the width of the surface gravity signal (resulting from the width of the jet).

M7. An analytical expression for the latitude of the wave source

Expanding on the physical intuition of the previous section here we derive an idealized analytical expression for the latitude of the wave source. Consider an idealized representation of the gravity anomaly resulting from the 21°N jet, shown in ED Fig. 6a-c (and ED Fig. 4i) in the form of a delta function in the form

$$\delta(x-c) \quad = \quad \sum_{n=0}^{\infty} a_n P_n(x), \tag{16}$$

where P_n are Legendre polynomials and $x = \sin\theta$ with θ being latitude. This is equivalent to Eq. 10 with a_n being proportional to J_n. Multiplying by $P_k(x)$, integrating and using orthogonality, leads to

$$a_k \quad = \quad \left(k+\frac{1}{2}\right) P_k(c). \tag{17}$$

The asymptotic limit of high-n gives then (Abramowitz & Stegun 8.10.7)

$$P_n(\sin\theta) \quad \sim \quad \cos\left[n\left(\frac{\pi}{2}-\theta\right)-\frac{\theta}{2}\right]. \tag{18}$$

Thus if the wave oscillates with a constant period then

$$n\left(\frac{\pi}{2}-\theta\right) \quad = \quad 2\pi. \tag{19}$$

Analyzing the oscillation in ED Fig. 6b shows a mean period of $n = 4.8667$ (for accuracy we extended the spectrum to very high harmonics and averaged the period), and taking this value in Eq. 19 gives $\theta = 16.03°$ in excellent agreement with ED Fig. 6a. Consistently as the north shift has a period of $n = 5.2222$ this gives in Eq. 19 $\theta = 21.06°$ and the south shift with a period of $n = 4.5625$ gives $\theta = 11.10°$, both very consistent with what we find in ED Fig. 6. This analysis is also consistent with treating the wind velocity as a delta function where similar oscillation frequencies and shift differences are found in Fig. 3.

Extended Data

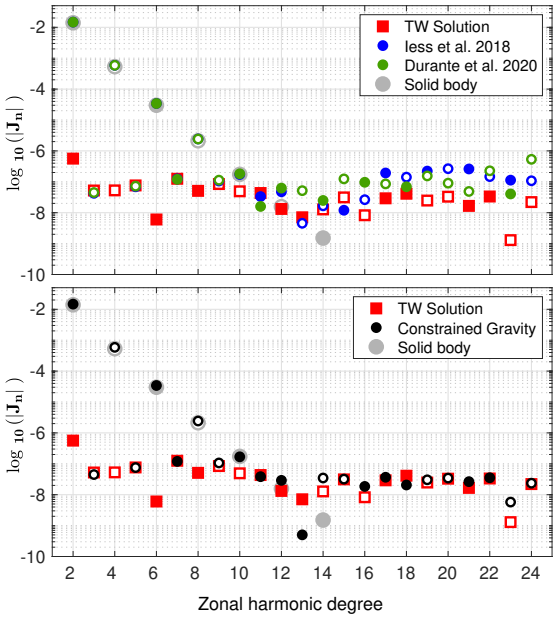

Extended Data Figure 1: Jupiter's measured and wind-induced calculated gravity harmonics ($J_2 - J_{24}$) in log-scale with positive (negative) values being in full (open) symbols. Top: the measured gravity harmonics based on the first two gravity orbits [9] (blue) and the first 10 gravity orbits [29] (green) compared to the calculated gravity harmonics resulting from the cloud-level winds using the thermal wind balance calculation [13] (red), and those arising from solid-body rotation alone [12] (gray). Bottom: The measured gravity harmonics using the constrained solution of this study (black) and the wind-induced gravity harmonics (red).

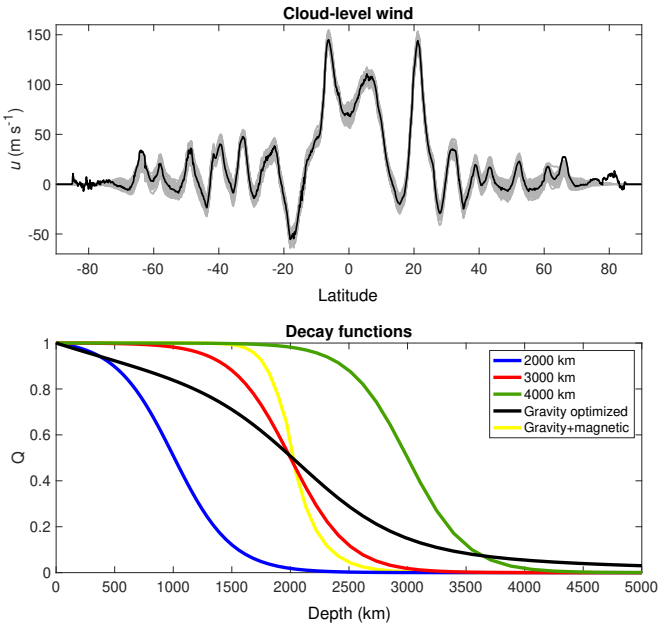

Extended Data Figure 2: Top: Jupiter's cloud level winds[20] (black) and their measurement uncertainty (gray) used for the calculation of the error bars in Fig. 2. Bottom: The vertical radial decay function for the cloud-level winds optimized for best matching J_3, J_5, J_7 and J_9 (black)[10], the simplified tanh functions used for the comparison in Fig. 3d (blue, red and green, corresponding to the colors in Fig. 3d), and the best fitting profile when including magnetic constraints[14] (yellow, in the context of this study it gives similar results to the red profile).

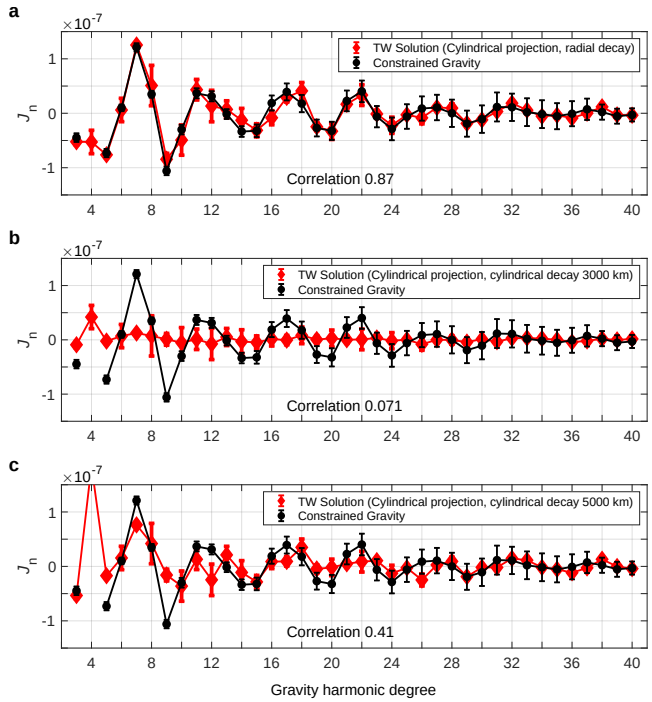

Extended Data Figure 3: a. Jupiter's measured gravity harmonics with the constrained solution (black) and the corresponding calculated wind-induced gravity harmonics based on projecting the cloud-level winds inward (red) cylindrically along the direction of the spin axis (a), as in Fig. 2 in the main text. **b.** A similar analysis, but with the wind decay being along the direction of the spin axis (z) instead of radially as done in the rest of the paper (using the same depth as in Fig. 2b). **c.** Same as (b), but with the decay being at 5000 km (the best optimized value).

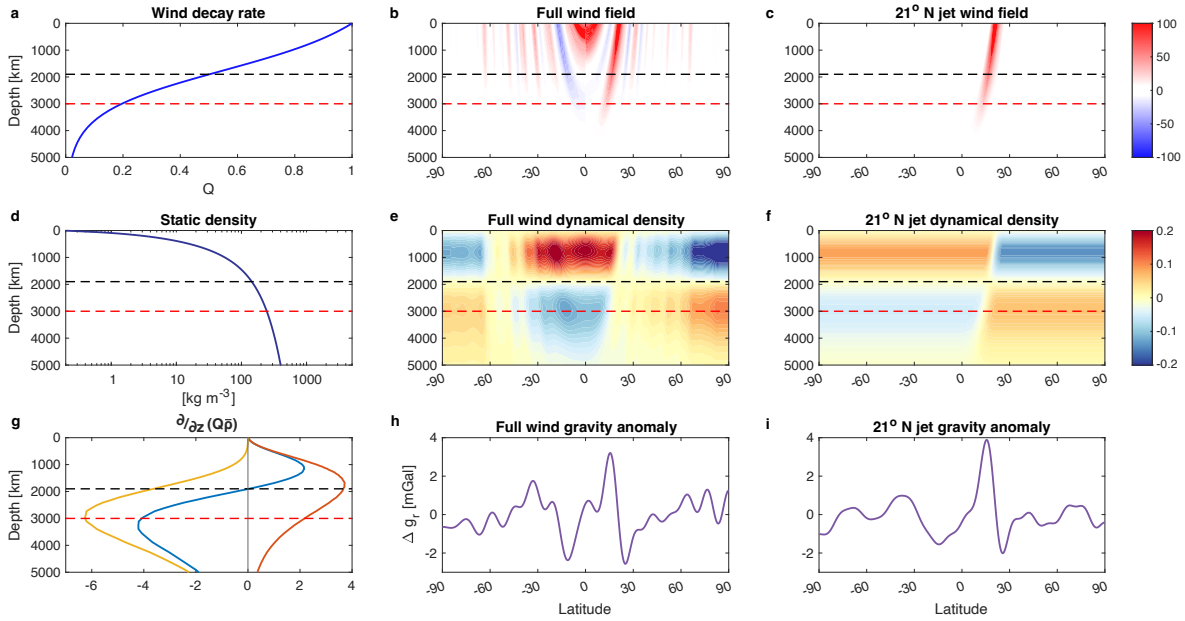

Extended Data Figure 4: a. The wind decay rate ($Q(r)$) as in ED Fig. 2 (black) used for both examined wind profiles in this figure. **b.** Jupiter's full wind field[20], $\mathrm{m\,s^{-1}}$, projected inward in a direction parallel to the axis of rotation, and decaying radially according to panel a. **c.** same as panel b, but with only the cloud-level jet of 21° N, $\mathrm{m\,s^{-1}}$. **d.** The static density component ($\bar{\rho}\,(r)$, $\mathrm{kg\,m^{-3}}$), which varies only with radius. **e. and f.** The dynamical density component (ρ', $\mathrm{kg\,m^{-3}}$) associated with the full wind field (panel b) and the 21° N jet (panel c) according to TW balance (8), respectively. **g.** The vertical shear of the multiplication of panels a and d ($\partial/\partial z(Q\bar{\rho})$, blue), the vertical shear of panel a ($\partial Q/\partial z$, yellow), and the vertical shear of panel d ($\partial\bar{\rho}/\partial z$, orange). **h. and i.** The gravitational anomaly, mGal, at the cloud-level, associated with the density field from panel e and f, respectively. The gravity anomaly was reconstructed with J_3, J_5, J_7, J_9 and J_{11-40}, see Eq. 10. **a-g.** The dashed black line represents a depth of about 1900 km from the cloud-level, where the vertical shear in panel g (blue) changes sign. Dashed red line represents the 3000 km depth, where the vertical shear of panel a ($\partial Q/\partial z$, yellow line in panel g) is minimal, representing the inflection depth.

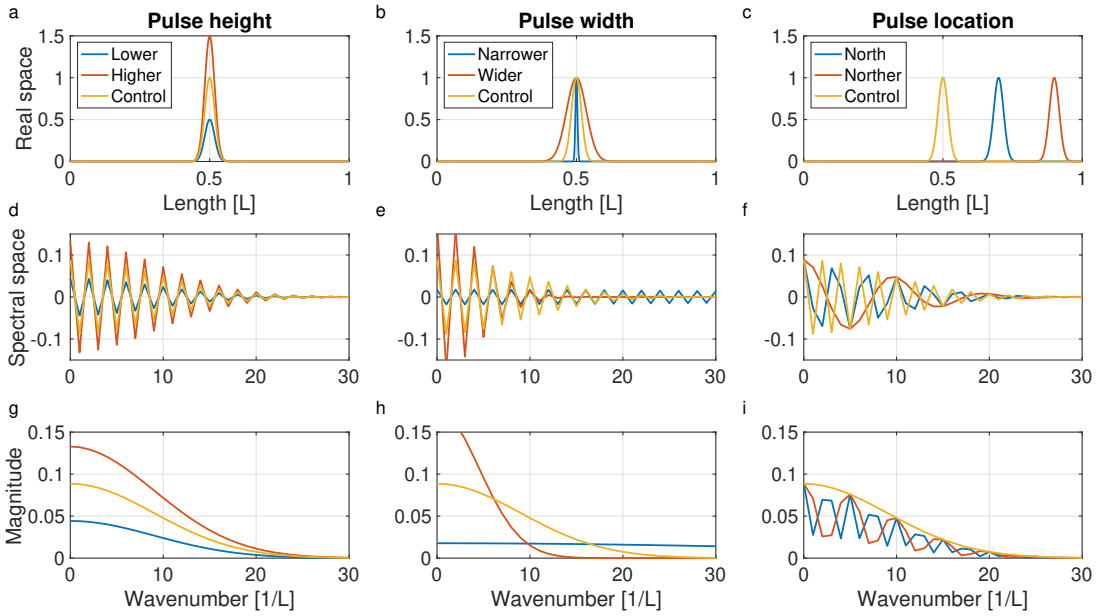

Extended Data Figure 5: A synthetic gaussian pulse represented using Fourier transform. Three tests are performed: different pulse heights (left panels), different pulse widths (middle panels), and different pulse locations (right panels). Each test is shown in the real space **a-c**, in spectral space **d-f**, and in a magnitude plot (absolute value) **g-i**. A control experiment is equivalent in all three cases (yellow). See text in M6 for further details.

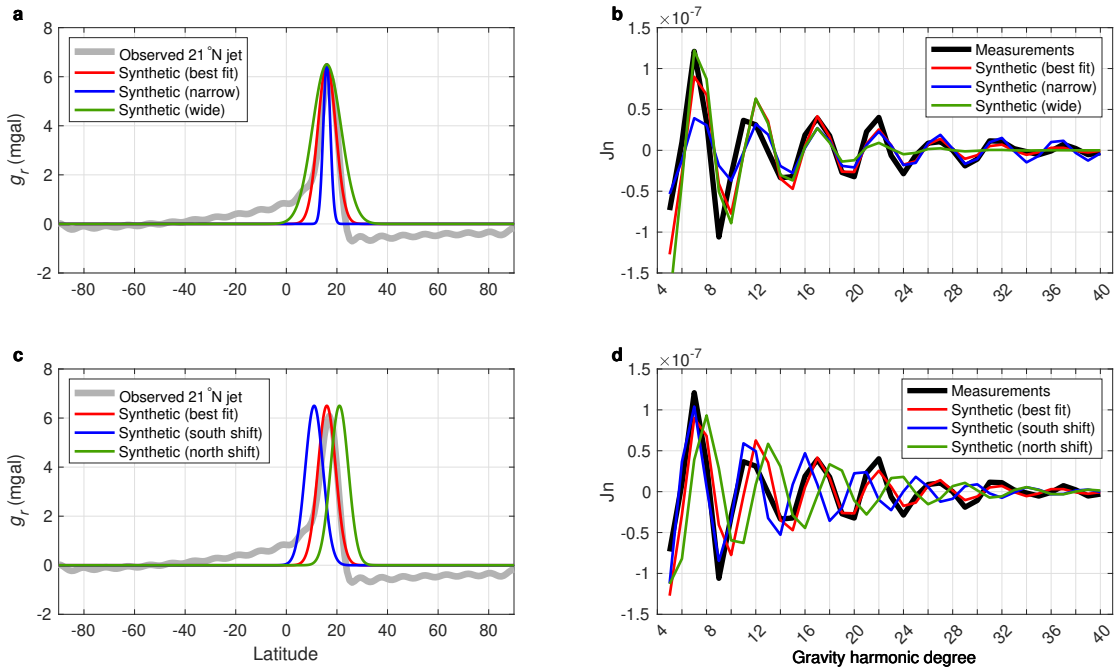

Extended Data Figure 6: The surface gravity signal and how it is expressed in the gravity harmonics. **a.** the surface gravity signal resulting from the 21°N observed jet (gray), and a simple synthetic gaussian function that fits best the observed values (red). Also shown are two variants, a narrower synthetic function (blue), and a wider synthetic function (green). **b.** the measured gravity harmonics (black), and the gravity harmonics calculated from the surface gravity shown in (a). **c.** same as upper panels, but for two other synthetic cases, with the surface gravity shifted poleward (green) and equatorward (blue) by 5°. **d.** the resulting gravity harmonics from (c).

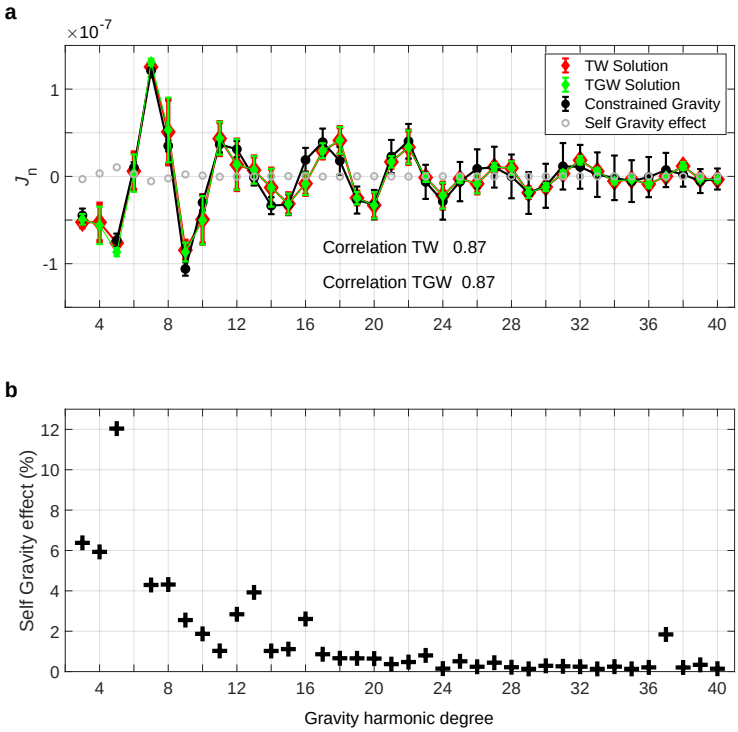

Extended Data Figure 7: a. Jupiter's measured gravity harmonics with the constrained solution (black), the corresponding calculated wind-induced gravity harmonics (red) based on projecting the cloud-level winds inward cylindrically along the direction of the spin axis as in Fig. 2 in the main text, and the solution including the self-gravity term as in Eq. 7, using the solution method of Wicht et al., 2020[49] (green). The difference between the two solutions is shown by the gray circles. The results are consistent with those of Wicht et al., 2020. **b.** The relative contribution of the self-gravity term to the gravity harmonics showing the contribution are overall small, particularly for the high-harmonics. The values of J_6 for both the TW and TGW are very close to zero (panel a), and thus the relative contribution is not meaningful and not shown in panel b.

J_n	Value ($\times 10^6$)	Uncertainty ($\times 10^6$)
J_2	14696.50743	0.00163
J_3	-0.04473	0.00263
J_4	-586.60657	0.00213
J_5	-0.07312	0.00253
J_6	34.19956	0.00203
J_7	0.12102	0.00249
J_8	-2.42483	0.00209
J_9	-0.10600	0.00257
J_{10}	0.16979	0.00295
J_{11}	0.03667	0.00305
J_{12}	0.03118	0.00308
J_{13}	-0.00149	0.00298
J_{14}	-0.03355	0.00324
J_{15}	-0.03220	0.00387
J_{16}	0.01883	0.00461
J_{17}	0.03922	0.00519
J_{18}	0.01784	0.00528
J_{19}	-0.02709	0.00516
J_{20}	-0.03230	0.00557
J_{21}	0.02274	0.00634
J_{22}	0.04023	0.00663
J_{23}	-0.00626	0.00652
J_{24}	-0.02867	0.00695
J_{25}	-0.00598	0.00751
J_{26}	0.00873	0.00742
J_{27}	0.01060	0.00780
J_{28}	0.00000	0.00836
J_{29}	-0.01904	0.00798
J_{30}	-0.01075	0.00840
J_{31}	0.01157	0.00888
J_{32}	0.01099	0.00837
J_{33}	0.00198	0.00850
J_{34}	-0.00163	0.00851
J_{35}	-0.00541	0.00798
J_{36}	-0.00081	0.00767
J_{37}	0.00733	0.00654
J_{38}	0.00217	0.00463
J_{39}	-0.00533	0.00458
J_{40}	-0.00300	0.00401

Extended Data Table 1: Estimated Jupiter zonal harmonics up to J_{40} based on the constraint solution and using Juno data collected from PJ01 to PJ37.

J_6	34.1880
J_8	-2.4608
J_{10}	0.2021

Extended Data Table 2: Values for solid-body J_n taken from interior structure models [12,13].